


# Simulation of gas-liquid two-phase flow in a flow-focusing microchannel with the lattice Boltzmann method

Kai Feng(冯凯), Gang Yang(杨刚), and Huichen Zhang(张会臣)
**Citation:**Chin. Phys. B, 2023, 32 (**11**): 114703. DOI: 10.1088/1674-1056/acea6e
Journal homepage: http://cpb.iphy.ac.cn; http://iopscience.iop.org/cpb

**What follows is a list of articles you may be interested in**

---

## Discussion on interface deformation and liquid breakup mechanism in vapor-liquid two-phase flow

Xiang An(安祥), Bo Dong(董波), Ya-Jin Zhang(张雅瑾), and Xun Zhou(周训)
Chin. Phys. B, 2023, 32 (**9**): 094702. DOI: 10.1088/1674-1056/acc78e

## Simulation of single bubble dynamic process in pool boiling process under microgravity based on phase field method

Chang-Sheng Zhu(朱昶胜), Bo-Rui Zhao(赵博睿), Yao Lei(雷瑶), and Xiu-Ting Guo(郭秀婷)
Chin. Phys. B, 2023, 32 (**4**): 044702. DOI: 10.1088/1674-1056/aca209

## Impact mechanism of gas temperature in metal powder production via gas atomization

Peng Wang(汪鹏), Jing Li(李静), Xin Wang(王欣), Bo-Rui Du(杜博睿), Shi-Yuan Shen(申世远), Xue-Yuan Ge(葛学元), and Miao-Hui Wang(王淼辉)
Chin. Phys. B, 2021, 30 (**5**): 054702. DOI: 10.1088/1674-1056/abd75e

## Effect of non-condensable gas on a collapsing cavitation bubble near solid wall investigated by multicomponent thermal MRT-LBM

Yu Yang(杨雨), Ming-Lei Shan(单鸣雷), Qing-Bang Han(韩庆邦), and Xue-Fen Kan(阚雪芬)
Chin. Phys. B, 2021, 30 (**2**): 024701. DOI: 10.1088/1674-1056/abbbf8

## Multi-bubble motion behavior of uniform magnetic field based on phase field model

Chang-Sheng Zhu(朱昶胜), Zhen Hu(胡震), Kai-Ming Wang(王凯明)
Chin. Phys. B, 2020, 29 (**3**): 034702. DOI: 10.1088/1674-1056/ab6839

---

# Simulation of gas–liquid two-phase flow in a flow-focusing microchannel with the lattice Boltzmann method

Kai Feng(冯凯), Gang Yang(杨刚), and Huichen Zhang(张会臣)†

*Naval Architecture and Ocean Engineering College, Dalian Maritime University, Dalian* 116026, *China*

(Received 12 June 2023; revised manuscript received 21 July 2023; accepted manuscript online 26 July 2023)

A lattice Boltzmann method for gas–liquid two-phase flow involving non-Newtonian fluids is developed. Bubble formation in a flow-focusing microchannel is simulated by the method. The influences of flow rate ratio, surface tension, wetting properties, and rheological characteristics of the fluid on the two-phase flow are analyzed. The results indicate that the flow pattern transfers from slug flow to dry-plug flow with a sufficiently small capillary number. Due to the presence of three-phase contact lines, the contact angle has a more significant effect on the dry-plug flow pattern than on the slug flow pattern. The deformation of the front and rear meniscus of a bubble in the shear-thinning fluid can be explained by the variation of the capillary number. The reduced viscosity and increased contact angle are beneficial for the drag reduction in a microchannel. It also demonstrates the effectiveness of the current method to simulate the gas–liquid two-phase flow in a microchannel.

**Keywords:** two-phase flow, lattice Boltzmann method, pressure drop, flow-focusing microchannel

**PACS:** 47.61.Jd, 47.11.Qr, 02.60.Cb **DOI:** 10.1088/1674-1056/acea6e

## 1. Introduction

Gas–liquid two-phase flow in a microchannel is of crucial importance in industrial applications. Extensive studies on the two-phase flow have been conducted.[1–3]

The flow pattern and pressure drop affect the dynamic characteristics of two-phase flow significantly. Different flow patterns can be obtained by controlling the gas–liquid flow rate.[4] Among all the flow patterns, slug flow attracts more attention because of its broad operating conditions and applications.[5,6] The formation of a bubble is under the combined effect of inertia force, viscous force, and surface tension. The capillary number is a vital parameter that affects the generation of bubbles.[7] The length of a bubble can be measured by image observation, which is found to be proportional to the gas–liquid flow rate ratio. The pressure drop gradient can be predicted by correlations based on the homogeneous and separated flow models.[8] To achieve higher prediction accuracy, the two-phase flow pattern should be considered.[9,10] The shear-thinning characteristics of the fluid affect the flow pattern and the pressure drop. The unique flow patterns are observed in the shear-thinning fluid.[11]

Numerical simulation gives information on the flow and pressure fields, which can supplement experimental research and explain the causes of physical phenomena. The lattice Boltzmann method (LBM) has potential applications in multiphase flow simulation because of its advantages of natural parallelism and dealing with complex boundaries. The color gradient[12] and pseudo-potential models[13] are developed to deal with the multiphase flow during the last three decades. Extensive studies have been carried out with these multiphase LBM. However, it is difficult to achieve a large density ratio because of the numerical instability. For a gas–liquid system, the density ratio is 1:800. The phase-field model is a useful tool to deal with the multiphase flow problems, which consists of the classic Navier–Stokes equations and the Cahn–Hilliard or Allen–Cahn equation.[14] With a suitable forcing scheme, the phase-field model can recover the full set of thermohydrodynamic equations for the nonideal fluids[15] and reduce the numerical dispersion.[16] Zheng *et al.*[17] proposed a phase-field model with a density ratio of 1:1000. In the phase-field model, two distribution functions are employed to calculate the flow field and capture the gas–liquid interface, respectively. It was developed to simulate the impact characteristics of the droplets by Ma *et al.*[18] However, the average gas–liquid density rather than the actual gas–liquid density is used in the model to calculate the Navier–Stokes equation, resulting in a difference in the pressure results with the natural gas–liquid system. Liang *et al.*[19] developed a new high-density ratio model with high numerical stability, which can reasonably simulate the gas–liquid system by setting a proper external force distribution function.

The two-phase flow pattern can be captured, while the formation mechanism of the flow pattern is not fully understood. The two-phase pressure drop can be measured on a macroscale and predicted with empirical correlations. However, the mechanism of pressure drop needs to be clarified. The phase-field LBM involving non-Newtonian fluid has not yet been used to simulate the two-phase flow in a flow-focusing junction. This study focuses on the bubble formation and pressure drop in a flow-focusing microchannel. The ef-

†Corresponding author. E-mail: hczhang@dlmu.edu.cn

© 2023 Chinese Physical Society and IOP Publishing Ltd 

fects of the gas–liquid flow rate ratio, surface tension, contact angle, and liquid rheological properties are discussed.

## 2. Number method

### 2.1. Phase-field LBM

The phase-field LBM improved by Liang *et al.*[19] is employed to handle the gas–liquid two-phase flow. The distribution function $g_i(x,t)$ is applied to capture the gas–liquid interface, and the evolution equation is given by

$$\begin{aligned} &g_i\left(\boldsymbol{x}+\boldsymbol{e}_i t, t+\delta_t\right)-g_i(\boldsymbol{x}, t) \\ &=-\frac{1}{\tau_g}\left[g_i(\boldsymbol{x}, t)-g_i^{\mathrm{eq}}(\boldsymbol{x}, t)\right]+\delta_t G_i(\boldsymbol{x}, t), \end{aligned} \tag{1}$$

where $g_i^{\mathrm{eq}}(x,t)$ is the equilibrium distribution function, $\tau_g$ is the relaxation parameter, and $G_i(x,t)$ is the force term. The equilibrium distribution function $g_i^{\mathrm{eq}}(x,t)$ is given by

$$g_i^{\mathrm{eq}}(x,t)=w_i\phi\left(1+\frac{\boldsymbol{e}_i\cdot\boldsymbol{u}}{c_{\mathrm{s}}^2}\right), \tag{2}$$

where $\boldsymbol{u}$ is the fluid velocity, $c_{\mathrm{s}}$ is the sound speed, $w_i$ are the weight factors, $w=4/9$, $w_{1-4}=1/9$, $w_{5-8}=1/36$, and $\boldsymbol{e}_i$ are the discrete velocity vectors to neighboring nodes. For a two-dimensional nine-velocity model, $\boldsymbol{e}_i$ are given by: $\boldsymbol{e}=(0,0)$, $\boldsymbol{e}_i=(\cos[(i-1)\pi/2],\ \sin[(i-1)\pi/2])c$, for $i=1$–4, and $\boldsymbol{e}_i=(\cos[(i-5)\pi/2+\pi/4],\ \sin[(i-5)\pi/2)+\pi/4])c$, for $i=5$–8, where $c$ is the lattice speed, $c=\delta x/\delta t$ ($\delta x$ and $\delta t$ are the lattice spacing and time, respectively). In the phase-field model, $\phi$ is the order parameter used to distinguish different fluid, which generally takes 1 and 0 in the liquid and gas bulk regions.

The force term $G_i(x,t)$ is given by

$$G_i=\left(1-\frac{1}{2\tau_g}\right)\frac{w_i\boldsymbol{e}_i\cdot\left[\partial_t(\phi\boldsymbol{u})+c_{\mathrm{s}}^2\lambda\boldsymbol{n}\right]}{c_{\mathrm{s}}^2}, \tag{3}$$

where $\lambda$ is a function of $\phi$, $\lambda=4\phi(1-\phi)/W$, $W$ is the interface thickness; $\boldsymbol{n}$ is the unit vector to the interface, $\boldsymbol{n}=\nabla\phi/|\nabla\phi|$; the relaxation parameter $\tau_g$ is determined by the mobility $M$, which can be written as

$$\tau_g=0.5+\frac{M}{c_{\mathrm{s}}^2\delta_t}. \tag{4}$$

The order parameter $\phi$ can be computed as

$$\phi=\sum_i^{g_i}. \tag{5}$$

The density of the two-phase flow is obtained by linear interpolation

$$\rho=\phi\left(\rho_{\mathrm{L}}-\rho_{\mathrm{G}}\right)+\rho_{\mathrm{G}}, \tag{6}$$

where the subscripts L and G are for liquid and gas phases, respectively.

The distribution function $f_i(x,t)$ is used for solving the flow field, and the evolution equation is written as

$$\begin{aligned} &f_i\left(\boldsymbol{x}+\boldsymbol{e}_i t, t+\delta_t\right)-f_i(\boldsymbol{x}, t) \\ &=-\frac{1}{\tau_f}\left[f_i(\boldsymbol{x}, t)-f_i^{\mathrm{eq}}(\boldsymbol{x}, t)\right]+\delta_t F_i(\boldsymbol{x}, t), \end{aligned} \tag{7}$$

where $F_i(x,t)$ is the force term, $f_i^{\mathrm{eq}}(x,t)$ is the equilibrium distribution function defined as

$$\boldsymbol{f}_i^{\mathrm{eq}}=\begin{cases}\dfrac{p}{c_{\mathrm{s}}^2}(w_i-1)+\rho s_i(\boldsymbol{u}), & i=0,\\ \dfrac{p}{c_{\mathrm{s}}^2}w_i+\rho s_i(\boldsymbol{u}), & i\neq 0,\end{cases} \tag{8}$$

with

$$s_i(\boldsymbol{u})=w_i\left[\frac{\boldsymbol{e}_i\cdot\boldsymbol{u}}{c_{\mathrm{s}}^2}+\frac{(\boldsymbol{e}_i\cdot\boldsymbol{u})^2}{2c_{\mathrm{s}}^4}-\frac{\boldsymbol{u}\cdot\boldsymbol{u}}{2c_{\mathrm{s}}^2}\right]. \tag{9}$$

The force term $F_i(x,t)$ is given by

$$\begin{aligned} F_i=&\left(1-\frac{1}{2\tau_f}\right)w_i\left[\boldsymbol{u}\cdot\nabla\rho+\frac{\boldsymbol{e}_i\cdot(\mu_\phi\nabla\phi+G)}{c_{\mathrm{s}}^2}\right.\\ &\left.+\frac{\boldsymbol{u}\nabla\rho:\left(\boldsymbol{e}_i\boldsymbol{e}_i-c_{\mathrm{s}}^2\boldsymbol{I}\right)}{c_{\mathrm{s}}^2}\right], \end{aligned} \tag{10}$$

where $G$ is body force, $\mu_\phi$ is the chemical potential, which can be calculated as

$$\mu_\phi=48\sigma\phi\left(\phi-1\right)\left(\phi-0.5\right)/W-1.5\sigma W\nabla^2\phi, \tag{11}$$

where $\sigma$ is the surface tension. In Eq. (7), and the relaxation parameter $\tau_f$ is determined by the kinematic viscosity $\nu$

$$\tau_f=0.5+\frac{\nu}{c_{\mathrm{s}}^2\delta_t}. \tag{12}$$

The viscosity of a gas–liquid two-phase system is not a constant value. Linear and inverse linear interpolations of the order parameter were used to determine the viscosity at the interface.[19,20] In present simulation, both the kinematic viscosity and density jump at the interface. To ensure the continuity of the interface, a linear interpolation of the order parameter is used to calculate the dynamic viscosity $\mu$ of the interface,

$$\mu(\phi)=\mu_{\mathrm{G}}+\phi(\mu_{\mathrm{L}}-\mu_{\mathrm{G}}). \tag{13}$$

The kinematic viscosity $\nu$ is obtained from the ratio of dynamic viscosity to density, $\nu=\mu/\rho$.

The velocity $\boldsymbol{u}$ and pressure $p$ are evaluated as

$$\boldsymbol{u}=\frac{1}{\rho}\left(\sum_{i=0}^{8}\boldsymbol{e}_i f_i(\boldsymbol{x},t)+0.5\delta_t\boldsymbol{F}\right), \tag{14}$$

$$p=\frac{c_{\mathrm{s}}^2}{1-w_0}\left[\sum_{i\neq 0}f_i+\frac{\delta_t}{2}\boldsymbol{u}\cdot\nabla\rho+\rho S_0(\boldsymbol{u})\right]. \tag{15}$$

### 2.2. LBM for non-Newtonian fluid

The dynamic viscosity for the non-Newtonian fluid is associated with the shear rate tensor. The simplest and most extensively used power-law model is employed to calculate the viscosity

$$\mu = k\dot{\gamma}^{n-1} = k\left[2\left(\boldsymbol{D}_{\alpha\beta} : \boldsymbol{D}_{\alpha\beta}\right)\right]^{(n-1)/2}, \tag{16}$$

where $k$ and $n$ are the consistency coefficient and the flow index, respectively, $\boldsymbol{D}_{\alpha\beta}$ is the strain rate tensor. The nonequilibrium part of the distribution function is used to obtain the shear rate tensor,[21,22] and the strain rate tensor can be calculated locally by

$$\boldsymbol{D}_{\alpha\beta} = -\frac{3}{2\rho\tau_f c^2}\sum_{i=0}^{8}\left(f_i - f_i^{\mathrm{eq}}\right)\boldsymbol{e}_{i\alpha}\boldsymbol{e}_{i\beta}, \tag{17}$$

where the subscripts $\alpha$ and $\beta$ are Cartesian coordinates.

The LBM becomes unstable for small relaxation time, and has poor accuracy for large relaxation time.[20] To achieve higher calculating accuracy and stability, the truncated power-law model[23] is adopted to set the range of the lattice kinematic viscosity ($0.001 \le \nu \le 3$). The truncated power-law model is given by

$$\nu(\dot{\gamma}) = \begin{cases} \nu_0, & \nu(\dot{\gamma}) < \nu_0, \\ \dfrac{k\dot{\gamma}^{n-1}}{\rho}, & \nu_0 \le \nu(\dot{\gamma}) \le \nu_\infty, \\ \nu_\infty, & \nu(\dot{\gamma}) > \nu_\infty. \end{cases} \tag{18}$$

The viscosity of a Newtonian fluid is constant. In contrast, the viscosity of a non-Newtonian fluid is not a uniform value. To represent the viscosity of the non-Newtonian fluid, the effective kinematic viscosity ($\nu_{\mathrm{eff}}$) is employed, which is given by

$$\nu_{\mathrm{eff}} = \frac{k}{\rho}\left(\frac{8u_{\mathrm{L}}}{D}\right)^{n-1}. \tag{19}$$

Here $D$ is the channel diameter, $u_{\mathrm{L}}$ is the superficial liquid velocity.

### 2.3. Wetting boundary condition

The contact angle $\theta_{\mathrm{c}}$ is used to characterize the wettability of the surface based on Young's equation,[24] which is calculated as

$$\cos\theta_{\mathrm{c}} = \frac{\sigma_{\mathrm{SG}} - \sigma_{\mathrm{SL}}}{\sigma}, \tag{20}$$

where the subscript G, L, and S represent the gas, liquid, and solid, respectively.

The schematic of the lattice nodes near the solid wall is shown in Fig. 1.

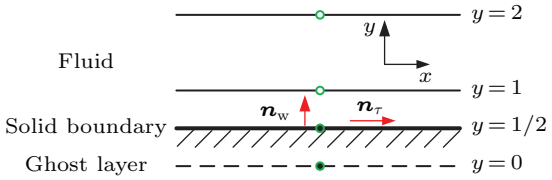



**Fig. 1.** Schematic diagram of the lattice nodes near the solid wall.

For discussing the three-phase contact line, the lattice nodes near the wall are divided into the fluid layer, solid boundary $y = 1/2$ and ghost layer $y = 0$.[25] According to the geometrical relation, the wetting boundary condition is given by[26]

$$\boldsymbol{n}_{\mathrm{w}} \cdot \nabla\phi = -\tan\left(\frac{\pi}{2} - \theta_{\mathrm{c}}\right)\left|\boldsymbol{n}_\tau \cdot \nabla\phi\right|, \tag{21}$$

where $\boldsymbol{n}_{\mathrm{w}}$ and $\boldsymbol{n}_\tau$ are the normal and tangential unit vectors, respectively; and $\boldsymbol{n}_{\mathrm{w}} \cdot \nabla\phi$ and $\boldsymbol{n}_\tau \cdot \nabla\phi$ are the normal and tangential components of $\nabla\phi$, respectively

$$\boldsymbol{n}_{\mathrm{w}} \cdot \nabla\phi = \frac{\phi_{x,1} - \phi_{x,0}}{\delta_x}, \tag{22}$$

$$\boldsymbol{n}_\tau \cdot \nabla\phi = \frac{\partial\phi_{x,1/2}}{\partial x} = 1.5\frac{\partial\phi_{x,1}}{\partial x} - 0.5\frac{\partial\phi_{x,2}}{\partial x}. \tag{23}$$

Here a second-order central difference approximation is used to calculate the derivatives of the order parameters

$$\frac{\partial\phi_{x,y}}{\partial x} = \frac{\partial\phi_{x+1,y} - \partial\phi_{x-1,y}}{2\partial x}. \tag{24}$$

## 3. Validation

The two-phase LBM and wetting boundary condition are validated by simulating the water droplets on solid surfaces with different wettability ($\theta_{\mathrm{c}} = 30°$–$150°$). A circular droplet is initially arranged on the bottom surface. The gas–liquid density ratio and kinematic viscosity ratio are set to 1:800 and 13:1, respectively. To weaken the numerical diffusion, the interface width $A$ is 5 lattice units. For numerical stability, the mobility $M$ and kinematic viscosity $\nu$ are set to: $M = 0.08$, $\nu_{\mathrm{L}} = 0.1$. For simplicity, the density of the gas phase is set to 1. The periodic boundary condition is imposed at the left and right boundaries, while the halfway bounce-back boundary condition is applied to the top and bottom boundaries. The wettability of the solid surface was approached by setting the normal component of the order parameter gradient (see Eqs. (21)–(24)).

The simulation domains are set to 120×48, 160×64, and 200×80. The corresponding initial droplet diameters are 36, 48, and 60 lattice units, respectively. Numerical simulations are conducted in different simulation domains. The simulation contact angles can be evaluated by $\theta_{\mathrm{sc}} = 2\arctan(2h/L)$, $L$ and $h$ are the spreading length and the height of the droplet, respectively.[25] The simulation contact angles $\theta_{\mathrm{sc}}$ at different simulation domains are list in Table 1.

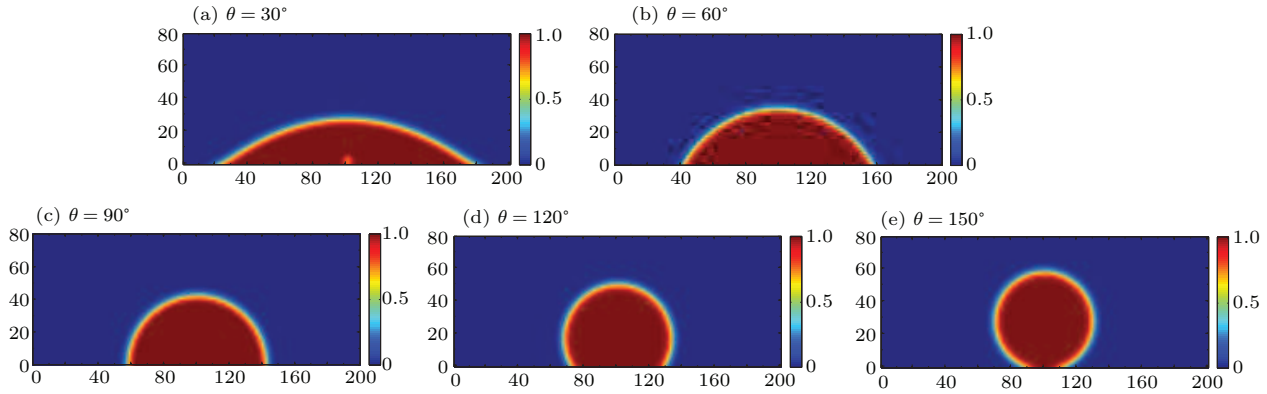



**Fig. 2.** Simulation results of droplet shapes for different contact angles.

**Table 1.** Simulation contact angle at different simulation domain.

| Theoretical contact angle ($\theta_{tc}$) | Simulation contact angle ($\theta_{sc}$) | | |
|---|---|---|---|
| | 120×48 | 160×64 | 200×80 |
| 30° | 32.5° | 32.1° | 32.0° |
| 60° | 61.2° | 60.6° | 60.6° |
| 90° | 89.6° | 91.0° | 91.0° |
| 120° | 121.° | 121.0° | 121.5° |
| 150° | 152.1° | 151.7° | 152.2° |

The simulation contact angle varies slightly with the variation of the simulation domain. The simulation contact angles agree with the theoretical values, with a root mean square error of 4.3%, 3.6%, and 3.5% for the simulation domains of 120×48, 160×64, and 200×80, respectively. It evidences that the wall contact angle can be well simulated by setting the wall order parameter gradient. In addition, the simulation domain of 200×80 can meet the calculation requirements. The simulation results of water drop shapes with different contact angles at the simulation domain of 200×80 are shown in Fig. 2.

In Fig. 2, the red part represents a water droplet ($\phi = 1$), and the blue part represents the gas phase ($\phi = 0$). A dot can be seen in the droplet near the channel wall in Fig. 2(a), while it is not a physical phenomenon. The simulation instability occurs in the initial droplet near the three-phase contact line, when $\theta_c = 30°$. Thus, a small area with $\phi < 1$ is observed at the three-phase contact line during calculation.

In our previous study, the truncated power-law model was validated by simulating the Poiseuille flow of the power-law fluids. In addition, it was employed to simulate the vortex characteristics of the non-Newtonian fluid.[27]

## 4. Results and discussion

The schematic of the flow-focusing microchannel is shown in Fig. 3. The gas phase is introduced from the left inlet, and the liquid phase enters the channel from the top and bottom inlets. The two-phase flow is formed at the junction and exits the channel through the right outlet.

For the physical gas–liquid system, the densities of the gas phase and water are 1.25 kg/m$^3$ and 1000 kg/m$^3$, respectively, at the room temperature of 20 °C. The gas–liquid density ratio is 1:800. The dynamic viscosities of the gas and liquid phases are 0.0159 mPa·s and 0.97 mPa·s, respectively.[4] The gas–liquid dynamic viscosity ratio is 1:61, and the gas–liquid kinematic viscosity ratio is 13:1 ($\nu = \mu/\rho$). In the LBM, the simulation parameters are: $\rho_G = 1$, $\rho_L = 800$, $\nu_L = 0.25$, $\nu_G = 3.25$, $M = 0.08$, $A = 5$, $\sigma = 30$. The velocities of the top and bottom liquid inlets are both 0.005. The superficial velocity of the gas inlet is 0.02. The contact angle of the solid wall is set to 90°. The velocity boundary condition is imposed at the inlets. The convective boundary condition is adapted for the outlet.[28]

Firstly, a grid-independence test is conducted. The widths of the microchannel are 30, 40, 50, and 60 lattice units, with corresponding simulation domains of 720×90, 960×120, 1200×150, and 1440×180. The dimensionless length of the bubble is used to compare the simulation results of different simulation domains, which is the ratio of the bubble length to the channel width. The dimensionless lengths of bubbles in different simulation domains are list in Table 2.

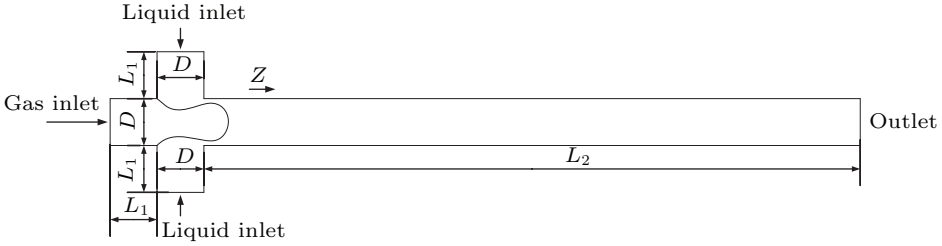



**Fig. 3.** Schematic diagram of the flow-focusing microchannel.

**Table 2.** Dimensionless width of the bubble with different simulation domains.

| Simulation domain | Width of the microchannel | Dimensionless width of the bubble |
|---|---|---|
| 720×90 | 30 | 1.3 |
| 960×120 | 40 | 1.6 |
| 1200×150 | 50 | 1.58 |
| 1440×180 | 60 | 1.59 |

When the simulation domain reaches 1200×150, the dimensionless length of the bubble remains almost unchanged as the simulation domain increases. It indicates that the simulation domain of 150×1200 is suitable for simulating the two-phase contact angle problems. The width of the microchannel ($D$) is 50 lattice units. The lengths of the inlets ($L_1$) are 50 lattice units, and the length of the outlet ($L_2$) is 1100 lattice units. Each lattice space corresponds to 6 μm.

Figure 4 shows the two-phase simulation flow pattern and the pressure along the centerline of the microchannel.

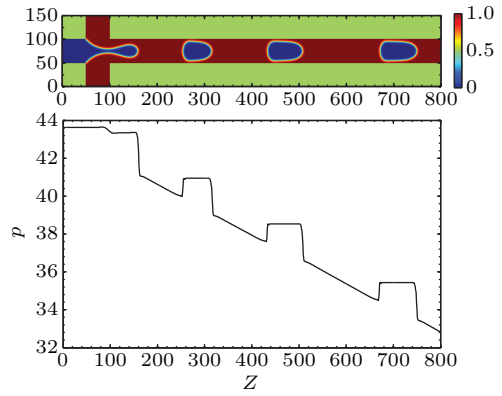



**Fig. 4.** Flow pattern and pressure along the centerline of the microchannel.

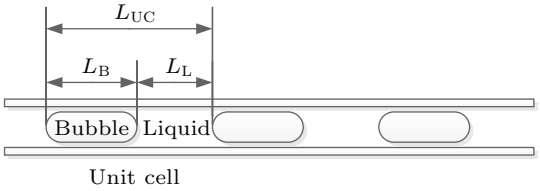



**Fig. 5.** Schematic plat of the unit cell model.

The slug bubbles are formed in the microchannel. In Fig. 4, the blue part represents bubbles ($\phi = 0$), and the red part represents the liquid phase ($\phi = 1$). The liquid film can be seen between the bubble and the channel wall. Corresponding to the two-phase flow pattern, the two-phase pressure drop includes the pressure drop across the bubble and the pressure drop of the liquid slug. The pressure drop gradient of the liquid slug is constant. In the liquid slug, the pressure in front of the bubble is lower than the pressure behind the bubble. This result is consistent with the unit cell model (see Fig. 5), which was employed to calculate the pressure drop of two-phase flow with the flow pattern information.[10]

The pressure drop gradient of a unit cell is calculated by

$$\left(\frac{\mathrm{d}p}{\mathrm{d}Z}\right)_{\mathrm{TP}} = \frac{p_{\mathrm{d}} + (\mathrm{d}p/\mathrm{d}Z)_{\mathrm{L}} L_{\mathrm{L}}}{L_{\mathrm{B}} + L_{\mathrm{L}}}, \tag{25}$$

where $(\mathrm{d}p/\mathrm{d}Z)_{\mathrm{L}}$ is the pressure drop gradient of the liquid slug, $p_{\mathrm{d}}$ is the pressure drop across the bubble, $L_{\mathrm{L}}$ and $L_{\mathrm{B}}$ are the lengths of the liquid slug and bubble, respectively.

The flow rate ratio, surface tension, wetting property, and rheological characteristics of the liquid phase impact the flow pattern and pressure drop significantly.

### 4.1. Effect of flow rate ratio

The gas–liquid flow rate ratio is a critical parameter in the flow pattern control. The contact angle of the solid wall is set to 90°. At a fixed velocity of the liquid phase 0.01 lattice units, the variation of flow rate ratios is achieved by changing the superficial gas velocity. The range of gas–liquid flow rate ratio $c$ is 1:1–3:1. Figure 6 shows the flow patterns at various flow rate ratios.

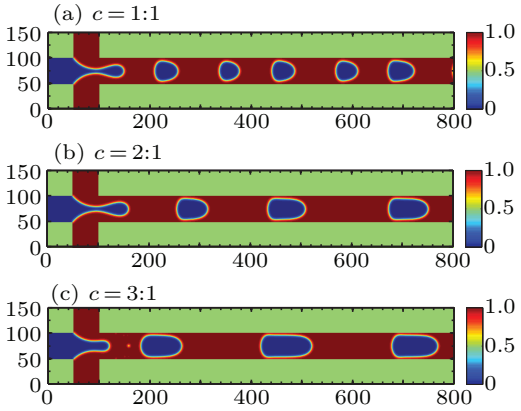



**Fig. 6.** Flow patterns at various flow rate ratios.

The bubble lengthens with the increase in the flow rate ratio. This agrees with the experimental results.[29] With a small capillary number, the surface tension dominates the viscous force. Thus, bubble generation is mainly controlled by the squeezing regime. The liquid pressure at the junction increases gradually with the liquid flowing into the microchannel from the inlet. When the pressure reaches the cut-off value, the bubble breaks under the squeeze force. The time for reaching the cut-off pressure is constant at a fixed liquid inlet velocity. For a larger flow rate ratio, more gas flows into the forming bubble, resulting in bubble lengthening.

The velocity of the liquid slug increases with the gas velocity, leading to the increase of the pressure drop across the bubble (see Fig. 7(a)). The expansion in liquid slug velocity also results in a rise in the pressure drop gradient in the liquid slug. Consequently, the two-phase pressure drop gradient increases with the flow rate ratio, as shown in Fig. 7(b).

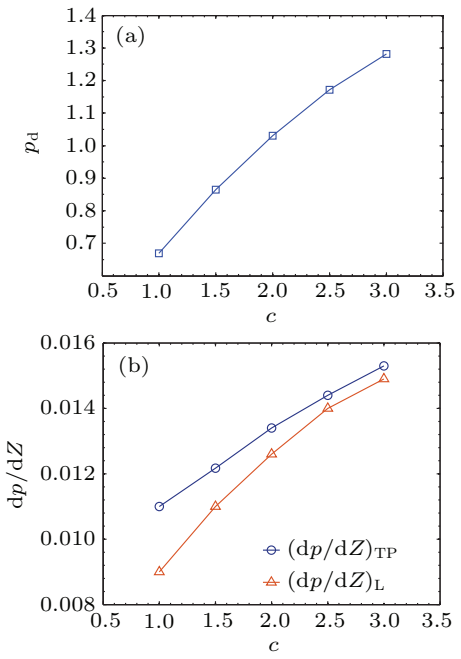



**Fig. 7.** Variation of pressure drop across the bubble (a) and pressure drop gradient (b) with the gas–liquid flow rate ratio.

### 4.2. Effect of surface tension

The surface tension of the fluid affects the bubble formation significantly. In the simulation, the superficial gas and liquid velocities are 0.02 and 0.01, respectively. The contact angle of the solid wall is set to 90°. The range of surface tension is 20–95.

Figure 8 shows the formation process of a slug bubble at $\sigma = 95$. The liquid film between the bubbles and the solid wall disappears. This flow pattern is named as the dry-plug flow by Heravi and Torabi.[30] The viscous force is insufficient to make the gas bubble deform. Thus, the forming bubble moves forward, occupying the cross-section of the microchannel after passing through the junction. The liquid accumulates at the intersection, leading to an expansion in the liquid pressure and the break of the forming bubble at the cross-junction. Similar flow patterns are also obtained by Yu *et al.*[31] and Shi *et al.*[32] at small capillary number. Similar to the dot in the contact angle simulation, the dots can be seen in the liquid in Fig. 8(d). The simulation instability occurs at the gas–liquid interface when the bubble breaks. Therefore, the small areas with $\phi < 1$ are observed in the liquid during calculation.

As the surface tension decreases, the capillary number increases, and the slug bubbles are formed in the microchannel at $\sigma = 50$, as shown in Fig. 9. The ratio of viscous force to surface tension increases, causing the deformation of the gas–liquid interface. The liquid film is formed. Therefore, the bubble can no longer occupy the channel's cross-section after passing through the junction. The squeeze force of the liquid at the cross-junction decreases. The bubble breaks at the right side of the junction under the combined effect of the shear and squeeze forces.

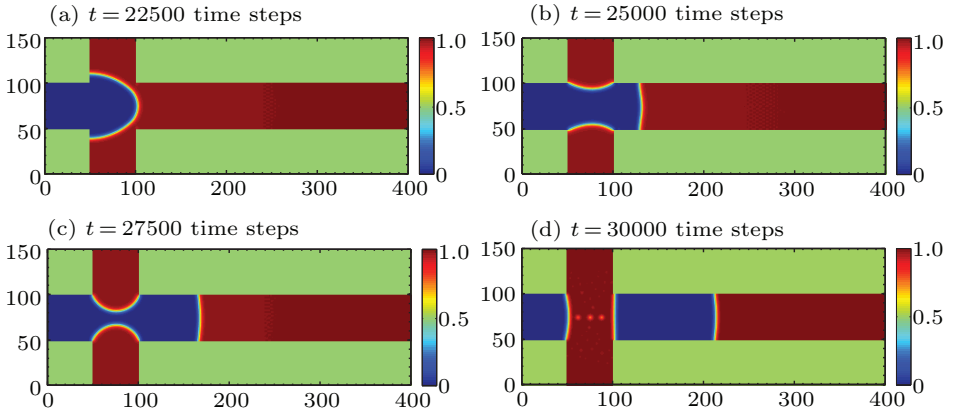



**Fig. 8.** Formation process of a dry-plug bubble at $\sigma = 95$.

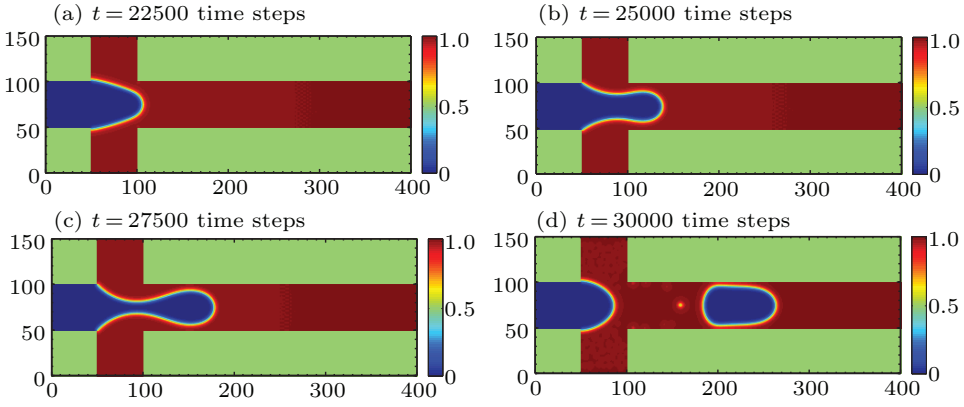



**Fig. 9.** Formation process of a slug bubble at $\sigma = 50$.

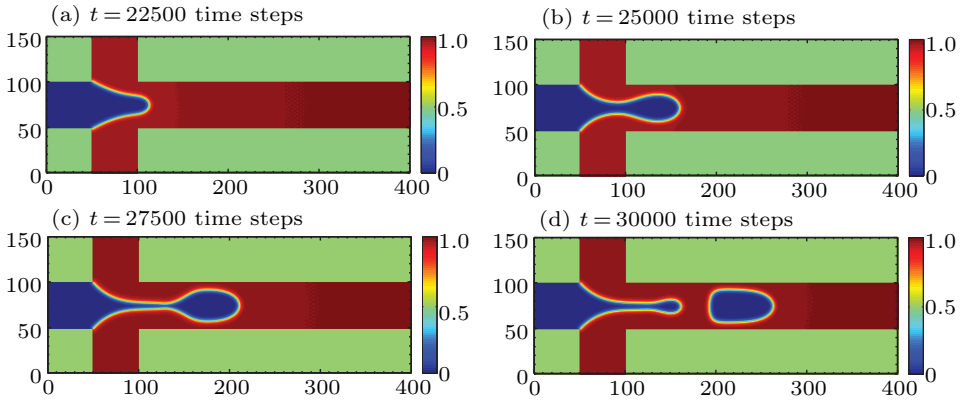



**Fig. 10.** Formation process of a slug bubble at $\sigma = 20$.

By reducing the surface tension, the capillary number is further increased. Figure 10 shows the bubble formation process in the microchannel at $\sigma = 20$.

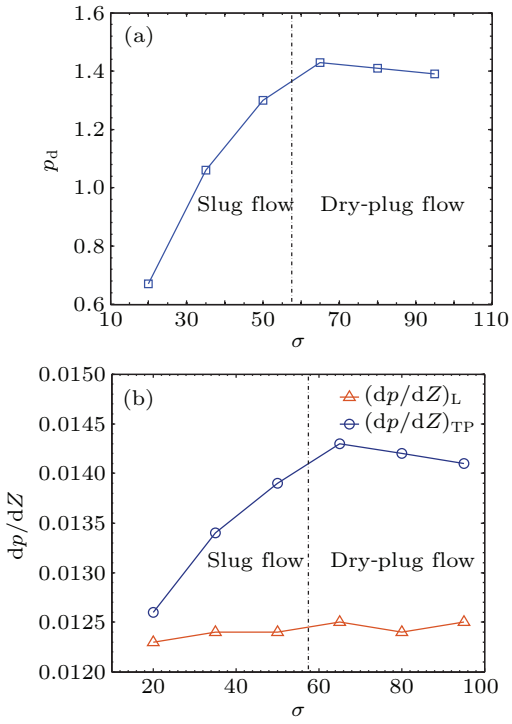



**Fig. 11.** Variation of pressure drop across the bubble (a) and pressure drop gradient (b) with surface tension.

With the increase of the *Ca*, the front of the bubble becomes sharper, while the rear becomes blunter. The variation of bubble shape depends on the pressure across the bubble $p_d$, which is related to the surface tension. Thus, the variation of the pressure drop with the surface tension needs to be clarified. The pressure drop across a slug bubble $p_d$ increases with the rise of the surface tension because $p_d$ is positively associated with surface tension,[8] which is expressed as

$$p_d = 7.16(3\mu u/\sigma)^{2/3}\sigma/D. \tag{26}$$

With the increase in $p_d$, the Laplace pressure across the rear meniscus decreases, while that across the front meniscus increases. Therefore, the rear curvature decreases, and the front curvature increases. Consequently, the front of the bubble becomes sharper, while the rear becomes blunter with the increase in *Ca*.

For the dry-plug flow, equation (26) is unsuitable for calculating $p_d$ due to the lack of liquid film. The pressure drop across a dry-plug is related to the three-phase contact line and the contact angle hysteresis.[30] Higher surface tension can hold the liquid slug together and reduce the pressure drop across the plug bubble. Consequently, as the surface tension increases, $p_d$ first increases and then decreases (see Fig. 11(a)).

The pressure drop gradient of the liquid slug is related to the fluid velocity and independent of the surface tension (see Fig. 11(b)). Thus, the relationship between the pressure drop gradient of the unit cell and the surface tension is consistent with the curve of the pressure difference across a bubble.

### 4.3. Effect of wetting property

The wetting property of the solid wall is characterized by the contact angle. Different contact angles ($\theta_c = 30°$–$150°$) can be obtained by adjusting the order parameter near the wall (see Eqs. (21)–(24)). The wettability affects the flow pattern and pressure drop of the two-phase flow by changing the three-phase contact line. The superficial gas and liquid velocities are 0.02 and 0.01, respectively. Due to the difference in three-phase contact conditions between slug flow and dry-plug flow, the effect of contact angle in these flow patterns are simulated.

Figure 12 shows the flow pattern of slug flow ($\sigma = 50$) at different contact angles.

The stable slug flow can be seen in the microchannel for all contact angles. No obvious three-phase contact line can be seen because of the liquid film. Thus, the contact angle has little influence on the flow pattern. Because $\theta_c$ has little effect on the flow pattern, $p_d$ is hardly affected by $\theta_c$ (see Fig. 13(a)). As $\theta_c$ increases, the drag reduction effect is more pronounced. Thus, $(dp/dZ)_L$ decreases with the increase in $\theta_c$. As a result, $(dp/dZ)_{TP}$ decreases with the increase in $\theta_c$ (see Fig. 13(b)).

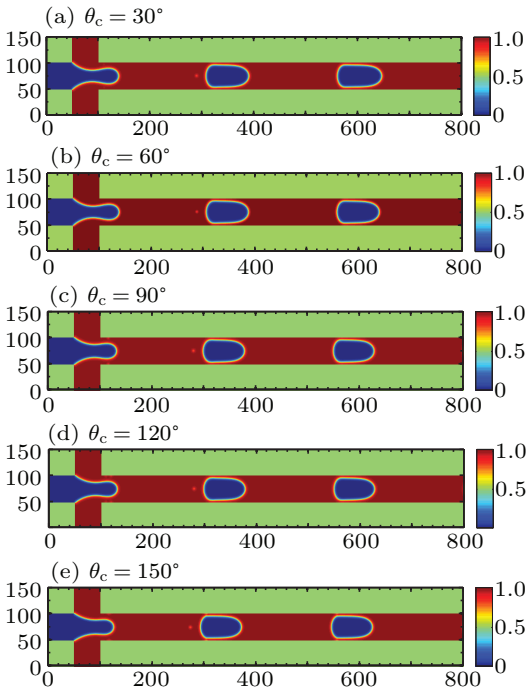



**Fig. 12.** Flow pattern of slug flow at different contact angles.

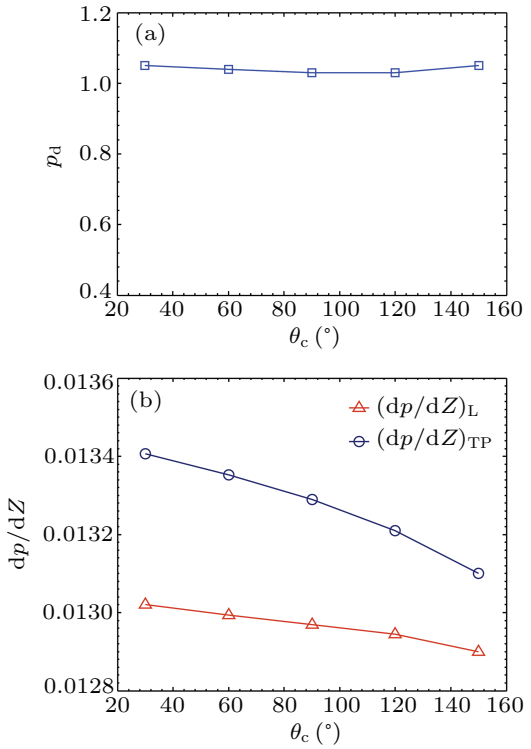



**Fig. 13.** Variation of pressure drop across the bubble (a) and pressure drop gradient (b) with the contact angle of slug flow.

The dry plug flow is obtained at $\sigma = 95$. The flow pattern of dry-plug flow under different wall contact angles is shown in Fig. 14.

There are apparent contact lines between the gas, liquid, and solid wall. The liquid film cannot be seen anymore. Therefore, the contact angle impacts the flow pattern significantly. With the rise of $\theta_c$, the flow pattern of the bubble changed from a convex shape to a concave shape gradually, and the transformation occurred at $\theta_c = 90°$.

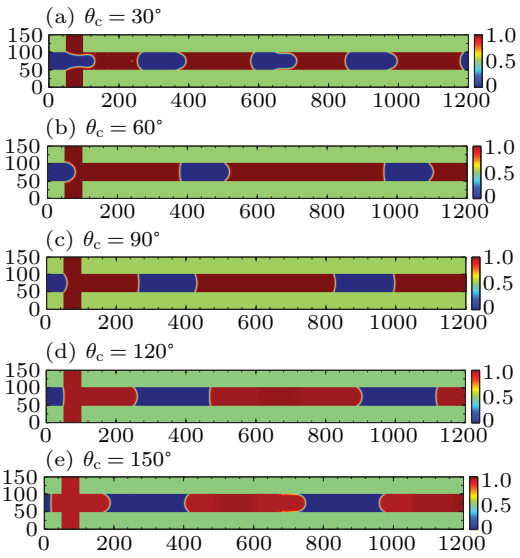



**Fig. 14.** Flow pattern of dry-plug flow with different contact angles.

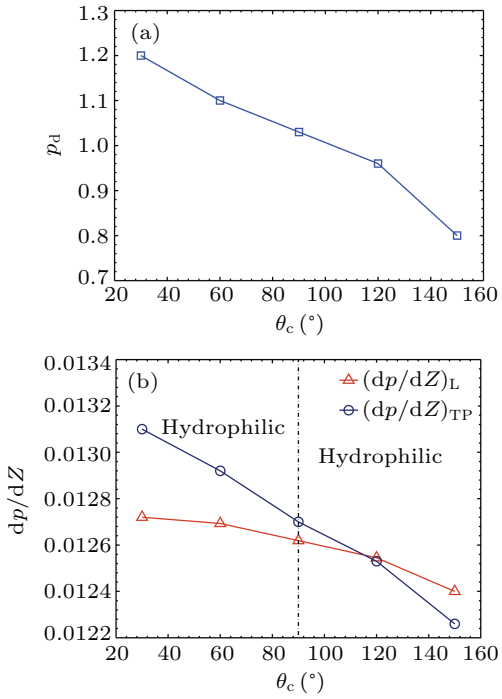



**Fig. 15.** Variation of pressure drop across the bubble (a) and pressure drop gradient (b) with the contact angle of dry-plug flow.

The convex curvature of the bubble front is greater than that of the rear. However, the concave curvature of the bubble front is less than the rear. These phenomena can be explained by the pressure of a two-phase flow. The relationship between the pressure across the gas–liquid interface and the curvature is determined by the Laplace formula. For the convex shape flow pattern, the pressure in the bubble is higher than in the liquid. Because of the pressure drop along the microchannel, the pressure in the fluid in front of the bubble is less than the pressure behind the bubble. In comparison, the pressure in the bubble is almost constant. The Laplace pressure at the bubble nose is greater than at the bubble rear, so the convex curvature of the bubble nose is larger than that of the bubble rear. For

the concave shape flow pattern, the pressure inside the bubble is lower than that in the liquid. The Laplace pressure at the bubble nose is less than that at the bubble rear. Thus, the concave curvature of the bubble front is less than that of the bubble rear.

The relationships between the pressure drop gradient in the liquid slug and the pressure drop across a dry-plug bubble with the contact angle are shown in Fig. 16. The contact angle hysteresis decreases with the rise in $\theta_c$. Therefore, the pressure drop across a dry-plug bubble falls with $\theta_c$ (see Fig. 15(a)). Because of the drag reduction effect of the hydrophobic surface, $(\mathrm{d}p/\mathrm{d}Z)_L$ decreases with $\theta_c$. Since both $p_d$ and $(\mathrm{d}p/\mathrm{d}Z)_L$ decrease with the rise in $\theta_c$, $(\mathrm{d}p/\mathrm{d}Z)_{TP}$ decreases with the increase in $\theta_c$ (see Fig. 15(b)). In particular, the pressure drop of the two-phase flow in the hydrophobic surface is slightly less than the pressure drop of the single-phase liquid.

### 4.4. Effect of non-Newtonian property of the liquid phase

The non-Newtonian property of the liquid plays an essential role in the two-phase flow pattern and pressure drop. Carboxymethyl cellulose (CMC) solution shows shear-thinning characteristics, which is widely used in industry. In the simulation, the CMC solutions with concentrations of 0.1%, 0.2%, and 0.3% (CMC 0.1, CMC 0.2, and CMC 0.3) are used. The physical properties of the CMC solutions are listed in Table 3.[4]

**Table 3.** Physical properties of the CMC solutions.

| Liquids | Density | Consistency | Flow index $n$ |
|---|---|---|---|
| | $\rho_p$ (kg/m$^3$) | coefficient $k_p$ (Pa·s$^n$) | |
| CMC 0.1 | 1000.8 | 0.086 | 0.63 |
| CMC 0.2 | 1001.7 | 0.218 | 0.57 |
| CMC 0.3 | 1002.3 | 0.422 | 0.53 |

In the simulation, the flow index is set to be the same as the physical properties. However, the consistency coefficient should be set according to the shear rate and the effective viscosity. The effective viscosities of the CMC 0.1, 0.2, and 0.3 can be calculated by Eq. (19). For the superficial liquid velocity of 0.1 m/s, the effective viscosities of the CMC 0.1, 0.2, and 0.3 are 4.66, 7.56, and 10.67 mPa·s. The simulation consistency coefficient of CMC solutions with different concentrations are determined according to the viscosity ratios of CMC solutions to water. Thus, the simulation consistency coefficient $k$ of the CMC 0.1, 0.2, and 0.3 are 89.33, 94.67, and 100.00. The superficial gas and liquid velocities are 0.02 and 0.01, respectively. The contact angles of the solid wall are set as 60°, 90°, and 120°.

The flow patterns in different fluids at $\theta_c = 90°$ are shown in Fig. 16.

With increased CMC solution concentration, the bubble front lengthens, and the bubble rear becomes flatter. This phenomenon has also been observed in some experiments, and it is explained to be associated with the shear-thinning characteristics of the liquid phase without detailed discussion.[4,11] In fact, it is related to the capillary number of the fluid. The effective viscosity increases with the increase in the CMC solution concentration, leading to increased capillary number. Therefore, the front of bubble turns sharper and longer, and the rear becomes flatter for a larger capillary number, which is discussed in Subsection 4.2.

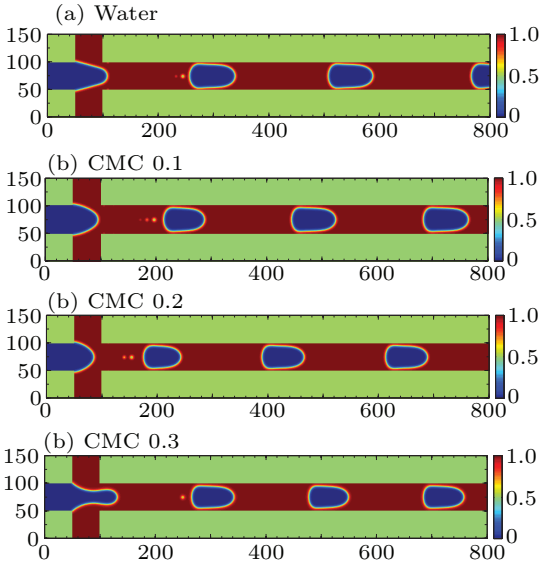



**Fig. 16.** Flow patterns in different fluids.

The variation of the pressure drop gradient in the liquid slug and the pressure drop across a bubble with the flow index at different contact angles are shown in Fig. 17.

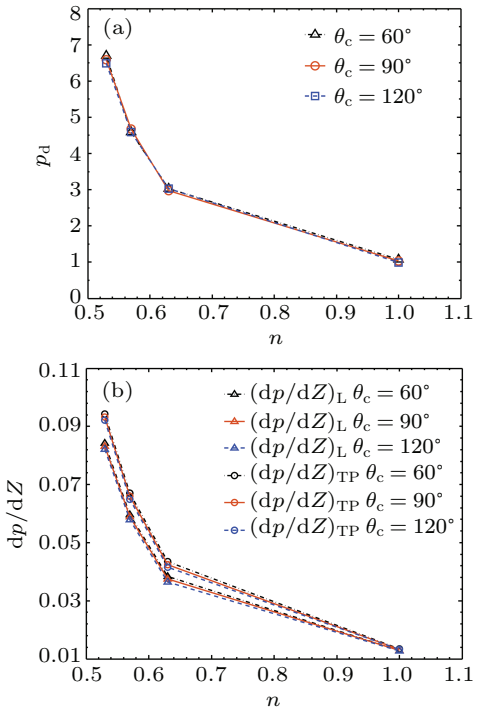



**Fig. 17.** Variation of pressure drop across the bubble (a) and pressure drop gradient (b) with flow index.

The effective viscosity of the liquid phase decreases with the increase in $n$, resulting in the reduction of $p_{\mathrm{d}}$ and $(\mathrm{d}p/\mathrm{d}Z)_{\mathrm{L}}$. Consequently, $(\mathrm{d}p/\mathrm{d}Z)_{\mathrm{TP}}$ decreases with the flow index. This is consistent with the experimental results.[4] Compared to rheological properties, the effect of $\theta_{\mathrm{c}}$ on pressure drop is relatively small. Due to the absence of three-phase contact line, the contact angle has almost no effect on $p_{\mathrm{d}}$, and $(\mathrm{d}p/\mathrm{d}Z)_{\mathrm{L}}$ slightly decreases with the increase in $\theta_{\mathrm{c}}$ because of the drag reduction in the hydrophobic surfaces. Therefore, $(\mathrm{d}p/\mathrm{d}Z)_{\mathrm{TP}}$ decreases with the increase in $\theta_{\mathrm{c}}$ slightly.

## 5. Conclusion

An LBM for gas–liquid two-phase flow involving non-Newtonian fluid is developed. The two-phase flow pattern and pressure drop are analyzed with this method, considering various parameters, including flow rate ratio, surface tension, wetting property, and rheological characteristics of the liquid phase. The numerical results agree well with the experimental results.

The bubble lengthens with a larger flow rate ratio. The flow pattern transfers from slug flow to dry-plug flow with a sufficiently small capillary number. For the slug flow, $\theta_{\mathrm{c}}$ has little effect on the flow pattern. However, for the dry-plug flow, the front and rear meniscus transfer from convex to concave gradually with the increase in $\theta_{\mathrm{c}}$. The transformation occurs at $\theta_{\mathrm{c}} = 90^{\circ}$. The two-phase flow pattern depends on the Laplace pressure across the gas–liquid interface. For the non-Newtonian fluid, the rear of the bubble becomes flatter, and the front becomes sharper for a small flow index, owing to the variation of the capillary number with the flow index. It also shows that the reduced viscosity and increased contact angle are beneficial for the drag reduction of two-phase flow in microchannel. In addition, this work validates the reliability of the developed LBM for simulating the gas–liquid two-phase flow in a microchannel. This method can be utilized to simulate the multiphase problems involving non-Newtonian fluids as well.

## Acknowledgement

Project supported by the National Natural Science Foundation of China (Grant No. 51775077).

## References

[1] Zhao C X and Middelberg A P J 2011 *Chem. Eng. Sci.* **66** 1394
[2] Zhang S, Zhu C, Feng H, Fu T and Ma Y 2021 *Chem. Eng. Sci.* **229** 116040
[3] Wang H, Liu L, Zhu C, Ma Y and Fu T 2022 *Chem. Eng. J.* **444** 136679
[4] Feng K and Zhang H 2021 *Chem. Eng. Res. Des.* **173** 158
[5] Sontti S G and Atta A 2017 *Ind. Eng. Chem. Res.* **56** 7401
[6] Saito S, Yoshino M and Suzuki K 2023 *Comput. Fluids* **254** 105797
[7] Zhang C, Fu T, Zhu C, Jiang S, Ma Y and Li H Z 2017 *Chem. Eng. Sci.* **172** 278
[8] Kawahara A, Yonemoto Y and Arakaki Y 2020 *Flow Turbul. Combust.* **105** 1325
[9] Bretherton F P 1961 *J. Fluid Mech.* **10** 166
[10] Kreutzer M T, Kapteijn F, Moulijn J A, Kleijn C R and Heiszwolf J J 2005 *AIChE J.* **51** 2428
[11] Mansour M H, Kawahara A and Sadatomi M 2015 *Int. J. Multiph. Flow* **72** 263
[12] Rothman D H and Keller J M 1988 *J. Stat. Phys.* **52** 1119
[13] Shan X and Chen H 1993 *Phys. Rev. E* **47** 1815
[14] Liu X, Chai Z, Zhan C, Shi B and Zhang W 2022 *Multiscale Model. Simul.* **20** 1411
[15] Liu X, Chai Z and Shi B 2023 *Phys. Rev. E* **107** 035308
[16] Wang H, Yuan X, Liang H, Chai Z and Shi B 2019 *Capillarity* **2** 33
[17] Zheng H W, Shu C and Chew Y T 2006 *J. Comput. Phys.* **218** 353
[18] Ma R, Zhou X, Dong B, Li W and Gong J 2018 *Int. J. Heat Fluid Flow* **71** 1
[19] Liang H, Xu J, Chen J, Wang H, Chai Z and Shi B 2018 *Phys. Rev. E* **97** 033309
[20] Dong B, Zhang Y, Zhou X, Chen C and Li W 2019 *Therm. Sci. Eng. Prog.* **10** 309
[21] Chai Z, Shi B, Guo Z and Rong F 2011 *J. Non-Newton. Fluid Mech.* **166** 332
[22] Chai Z and Zhao T S 2012 *Phys. Rev. E* **86** 016705
[23] Gabbanelli S, Drazer G and Koplik J 2005 *Phys. Rev. E* **72** 046312
[24] Young T 1805 *Philos. Trans. R. Soc.* **95** 65
[25] Liang H, Liu H, Chai Z and Shi B 2019 *Phys. Rev. E* **99** 063306
[26] Ding H and Spelt P D M 2007 *Phys. Rev. E* **75** 046708
[27] Feng K and Zhang H 2020 *Int. J. Mod. Phys. C* **32** 2150036
[28] Lou Q, Guo Z and Shi B 2013 *Phys. Rev. E* **87** 063301
[29] Fu T, Ma Y, Funfschilling D and Li H Z 2011 *Microfluid Nanofluid* **10** 1135
[30] Heravi P and Torabi F 2016 *Int. J. Multiph. Flow* **87** 9
[31] Yu Z, Hemminger O and Fan L 2007 *Chem. Eng. Sci.* **62** 7172
[32] Shi Y, Tang G H and Xia H H 2014 *Comput. Fluids* **90** 155